PHYSICAL REVIEW E **94**, 032212 (2016)

Dynamical indicators for the prediction of bursting phenomena in high-dimensional systems

Mohammad Farazmand and Themistoklis P. Sapsis
Department of Mechanical Engineering, Massachusetts Institute of Technology, 77 Massachusetts Avenue, Cambridge, Massachusetts 02115, USA

(Received 7 April 2016; revised manuscript received 19 July 2016; published 14 September 2016)

Drawing upon the bursting mechanism in slow-fast systems, we propose indicators for the prediction of such rare extreme events which do not require *a priori* known slow and fast coordinates. The indicators are associated with functionals defined in terms of optimally time-dependent (OTD) modes. One such functional has the form of the largest eigenvalue of the symmetric part of the linearized dynamics reduced to these modes. In contrast to other choices of subspaces, the proposed modes are flow invariant and therefore a projection onto them is dynamically meaningful. We illustrate the application of these indicators on three examples: a prototype low-dimensional model, a body-forced turbulent fluid flow, and a unidirectional model of nonlinear water waves. We use Bayesian statistics to quantify the predictive power of the proposed indicators.

DOI: 10.1103/PhysRevE.94.032212

I. INTRODUCTION

Complex irregular behavior is a characteristic of chaotic systems, which is usually visualized through the time series of an observable. Many natural and engineering systems exhibit a second level of complexity typified by rare extreme bursts in the time series of certain observables. They are rare in the sense that they are short-lived and the frequency at which they occur is significantly smaller than the typical frequency of the time series; and they are extreme in the sense that they correspond to the values of the observable that are several standard deviations away from its mean value. Examples of such rare, extreme phenomena in nature include oceanic rogue waves [1,2], intermittent fluctuations in turbulent models [3–5], and extreme events in climate dynamics [6,7]. While the prediction of extreme events is of utmost importance, our dim understanding of their origins and precursors has impeded our ability to predict them.

A promising approach is to predict the rare events directly from the time series of the observable. If the system has a compact, finite-dimensional attractor, the dynamics can, in principle, be reconstructed from the observations by delay-coordinate embedding techniques [8–10] or linear and/or nonlinear order reduction methods [11–15]. However, for high-dimensional chaotic attractors the reconstructed dynamics have a poor forecasting skill (see, e.g., [15,16]) which is comparable with mean-square models (models based on carefully tuned Langevin equations [17]). Since rare extreme events are associated with strong nonlinearities and intermittently positive Lyapunov exponents (i.e., high sensitivity to perturbations), their prediction from a finite set of observations is challenging and remains an active area of research (see, e.g., Giannakis and Majda [18] and Bialonski *et al.* [19]).

A more physically illuminating approach comes from multiscale analysis, where a dynamical system model is decomposed into slow and fast variables [20–24]. The bursting mechanism in these models is rather well understood [25,26]. For the most part, the dynamics takes place on the slow manifold. The slow dynamics may be chaotic, but no bursting event occurs on the slow manifold itself. The bursts occur along the unstable manifold (of the slow manifold) and correspond to the growth of the fast variables. The unstable manifold is typically homoclinic to the slow manifold such that the flow returns eventually to the slow manifold [27]. This cycle can repeat indefinitely and, if the slow dynamics is chaotic, irregularly (see Fig. 1, for an illustration).

While this geometric approach is certainly illuminating, it is of little applicability to complex systems, since a clear separation of time scales is often not available in realistic models (e.g., Navier-Stokes equations). Nor does there exist a general recipe to transform the coordinates into slow and fast variables [28]. This becomes particularly prohibitive in high-dimensional systems.

Here we introduce a diagnostic indicator for the prediction of rare extreme events in high-dimensional systems. The indicator is based on the aforementioned observations on the multiscale systems but does not require *a priori* known fast-slow coordinates. More precisely, we show that a small number of optimally time-dependent (OTD) modes [29], obtained through a minimization principle and the history of the system state up to the current time instant, allows for the description of the currently most unstable subspace in a dynamically consistent fashion. We show that the linearized dynamics projected in this optimal, time-dependent subspace can predict an upcoming rare extreme event. We note that simply computing the eigenvalues of the linearized dynamics is costly and, in many cases, the results are completely oblivious to transient instabilities (e.g., instabilities associated with non-normal dynamics [29]).

Going beyond visual inspections, we quantify the forecast skill of the indicators by examining the conditional statistics of the rare events. More precisely, using the Bayesian formula, we compute the probability of a future rare event, given the value of the indicator at the present time. For indicators with predictive power, the resulting conditional probability density functions exhibit a "bimodal" structure separating regular dynamics from extreme events.

In Sec. II, we review the OTD modes and introduce our indicator. We demonstrate the application of the indicator on three examples: a low-dimensional prototype system (Sec. III), a body-forced Navier-Stokes equation (Sec. IV), and a modified nonlinear Schrödinger equation as a model for unidirectional water waves (Sec. V). The concluding remarks are presented in Sec. VI.

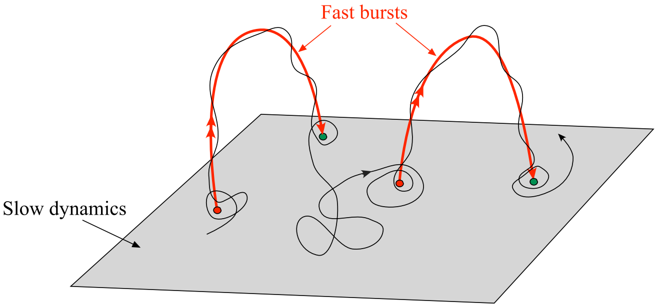

FIG. 1. An illustration of slow-fast systems with bursting orbits homoclinic to the slow manifold. While we depict the slow manifold with a plane, it can in reality be a complicated high-dimensional manifold.

II. PRELIMINARIES

A. Setup

Consider the general nonlinear system of ordinary differential equations (ODEs),

$$\dot{\mathbf{u}} = \mathbf{F}(\mathbf{u}), \quad \mathbf{u} \in \mathbb{R}^n, \tag{1}$$

where the vector field $\mathbf{F} : \mathbb{R}^n \to \mathbb{R}^n$ is sufficiently smooth. We denote the solutions of (1) with the initial condition $\mathbf{u}_0$ at time t_0 by $\mathbf{u}(t;t_0,\mathbf{u}_0) = \varphi_{t_0}^t(\mathbf{u}_0)$, where $\varphi_{t_0}^t$ is the flow map. Infinitesimal perturbations around an arbitrary trajectory $\mathbf{u}(t)$ satisfy the linear equation of variations

$$\dot{\mathbf{v}} = \mathbf{L}_{\mathbf{u}}\mathbf{v}, \quad \mathbf{v} \in \mathbb{R}^n, \tag{2}$$

where $\mathbf{L}_{\mathbf{u}(t)} := \nabla\mathbf{F}(\mathbf{u}(t))$. For notational simplicity, we write $\mathbf{L}$ instead of $\mathbf{L}_{\mathbf{u}}$.

For a given trajectory $\mathbf{u}(t;t_0,\mathbf{u}_0)$, there exists a two-parameter family of linear maps $\Phi_{t_0}^t(\mathbf{u}_0) : \mathbb{R}^n \to \mathbb{R}^n$ such that the solutions of the linear equation (2) satisfy $\mathbf{v}(t;t_0,\mathbf{v}_0) = \Phi_{t_0}^t(\mathbf{u}_0)\mathbf{v}_0$ [30]. For notationally simplicity, we denote the solutions of the equation of variations (2) by $\mathbf{v}(t)$ and write $\mathbf{v}(t) = \Phi_{t_0}^t\mathbf{v}_0$ along a given trajectory $\mathbf{u}(t) = \mathbf{u}(t;t_0,\mathbf{u}_0)$ of the nonlinear system (1).

In order to introduce the OTD modes, we need the following definition.

Definition 1. A time-dependent r-dimensional subspace $E_r(t)$ of $\mathbb{R}^n$ is *flow invariant* under the system (2) if, for a fixed initial time t_0, we have

$$\mathbf{v}(t) = \Phi_{t_0}^t\mathbf{v}_0 \in E_r(t), \quad \forall\ \mathbf{v}_0 \in E_r(t_0), \quad \forall\ t \geqslant t_0. \tag{3}$$

B. Optimally time-dependent modes

For $r = n$ in Definition 1, we have $E_n(t) = \mathbb{R}^n$ for all t and therefore the space is trivially flow invariant. Lower-dimensional flow-invariant subspaces can, in principle, be constructed as follows. Consider a prescribed set of r vectors $\{\mathbf{v}_1(t_0),\ldots,\mathbf{v}_r(t_0)\}$ spanning an r-dimensional subspace $E_r(t_0)$. For any later time $t > t_0$, let $\mathbf{v}_i(t)$ be the solutions of the liner equation (2) with the initial condition $\mathbf{v}_i(t_0)$ and define $E_r(t) = \operatorname{span}\{\mathbf{v}_1(t),\ldots,\mathbf{v}_r(t)\}$. If the vector field $\mathbf{F}$ is at least once continuously differentiable, the map $\Phi_{t_0}^t$ is a bijection, and therefore the dimension of the linear subspace $E_r(t)$ is equal to r for all $t \geqslant t_0$. Moreover, the subspaces $E_r(t)$, constructed as such, are flow invariant by definition.

This procedure is, however, known to be numerically unstable: Typically, the lengths of the vectors $\mathbf{v}_i$ grow exponentially fast and the angle between them vanishes rapidly. As a result, many numerical techniques have been introduced to compute the flow-invariant subspace in a numerically robust fashion (see, e.g., Greene and Kim [31] and Dieci and Elia [32]).

The OTD equations, introduced recently by Babaee and Sapsis [29], constitute a modification to the equation of variations (2) such that its solutions (the OTD modes) remain orthonormal for all times, yet they span the same flow-invariant subspaces as the solutions of the equation of variations.

Here we briefly review the OTD equations and the main properties of their solutions, referring the interested reader to [29] for details. The OTD equations read

$$\dot{\mathbf{v}}_i = \mathbf{L}_{\mathbf{u}}\mathbf{v}_i - \sum_{k=1}^{r}\langle\mathbf{L}_{\mathbf{u}}\mathbf{v}_i,\mathbf{v}_k\rangle\mathbf{v}_k, \quad i \in \{1,2,\ldots,r\}, \tag{4}$$

where $\langle\cdot,\cdot\rangle$ denotes an appropriate inner product and $1 \leqslant r \leqslant n$ is some prescribed integer. Equation (4), together with the original system (1), form a set of $(r+1)$ coupled nonlinear differential equations for vectors $\mathbf{v}_i \in \mathbb{R}^n$ and the state $\mathbf{u}$. Note that without the summation term, the OTD equation (4) coincides with the equation of variations (2). The summation terms impose the constraint that the solutions $\mathbf{v}_i$ remain orthonormal with respect to the inner product $\langle\cdot,\cdot\rangle$.

We refer to the solutions $\mathbf{v}_i$ of the OTD equation as the *OTD modes*, which have the following appealing properties.

(i) The OTD equations preserve orthonormality: Let the initial condition for the OTD equation (4) be a set of orthonormal vectors $\{\mathbf{v}_1(t_0),\mathbf{v}_2(t_0),\ldots,\mathbf{v}_r(t_0)\}$. Then the solution $\{\mathbf{v}_1(t),\mathbf{v}_2(t),\ldots,\mathbf{v}_r(t)\}$ of the OTD equation remains orthonormal for all times t [see 29, Theorem 2.1].

(ii) The OTD modes span flow-invariant subspaces: Define

$$E_r(t) = \operatorname{span}\{\mathbf{v}_1(t),\mathbf{v}_2(t),\ldots,\mathbf{v}_r(t)\}, \tag{5}$$

with $\{\mathbf{v}_1(t),\mathbf{v}_2(t),\ldots,\mathbf{v}_r(t)\}$ being an orthonormal solution of the OTD equation (4). Then the subspaces $E_r(t)$ are flow invariant under the linear system (2) [see 29, Theorem 2.4].

(iii) If $\mathbf{u}$ is a hyperbolic fixed point, the OTD modes generically converge to the subspace spanned by the r least-stable eigenvectors of $\mathbf{L}_{\mathbf{u}}$ [see 29, Theorem 2.3].

Figure 2 illustrates the geometry of OTD modes for $r = 2$. Note that evaluating the OTD modes requires the simultaneousness evolution of the OTD equation (4) and the

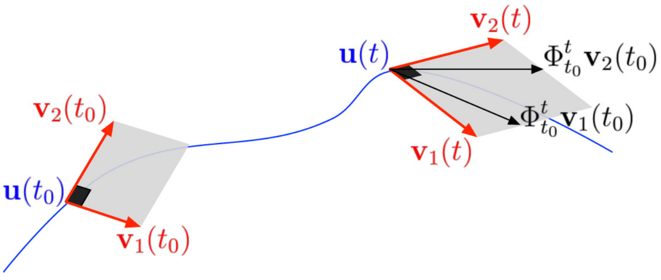

FIG. 2. An illustration of the OTD modes. The OTD modes $\mathbf{v}_i$ remain orthonormal for all times (the dark black squares mark right angles). While differing from their images under the linear dynamics $\Phi_{t_0}^t$, the OTD modes span the same subspace as their images.

original system (1), which together form a coupled nonlinear system of $(n + r \times n)$ equations.

C. Reduction to the OTD modes

Due to the flow invariance of the OTD modes, we can reduce the linear operator $\mathbf{L}_{\mathbf{u}}$ to the OTD subspaces $E_r(t)$ in a dynamically consistent fashion. More precisely, consider the solutions of the form $\mathbf{v}(t) = \mathbf{V}(t)\boldsymbol{\eta}(t)$, where $\mathbf{V} = [\mathbf{v}_1|\mathbf{v}_2|\cdots|\mathbf{v}_r] \in \mathbb{R}^{n\times r}$ is the time-dependent matrix whose columns are the OTD modes obtained from (4). The vector $\boldsymbol{\eta} \in \mathbb{R}^r$ is the solution $\mathbf{v}$ expressed in the OTD basis.

Substituting $\mathbf{v}(t) = \mathbf{V}(t)\boldsymbol{\eta}(t)$ in (2) yields the *reduced linear equation*

$$\dot{\boldsymbol{\eta}} = \mathbf{V}^{\dagger}\mathbf{L}\mathbf{V}\boldsymbol{\eta}. \tag{6}$$

Conversely, if $\boldsymbol{\eta}(t)$ solves the reduced equation (6), then $\mathbf{v}(t) = \mathbf{V}(t)\boldsymbol{\eta}(t)$ solves the full linear equation (2) [see 29, Theorem 2.4]. We refer to the linear map $\mathbf{L}_r : \mathbb{R}^r \to \mathbb{R}^r$,

$$\mathbf{L}_r(t) := \mathbf{V}^{\dagger}(t)\mathbf{L}(t)\mathbf{V}(t), \tag{7}$$

as the *reduced linear operator*.

The reduced system (6) is a linear system of differential equations with a time-dependent stability matrix $\mathbf{L}_r(t)$. As a result, the eigenvalues of $\mathbf{L}_r$ may not be used to assess linear growth or decay of perturbations. Instead, we use the invariants of the symmetric part of $\mathbf{L}_r$ as an indicator.

It follows from (6) that

$$\frac{1}{2}\frac{d}{dt}|\boldsymbol{\eta}|^2 = \langle \boldsymbol{\eta}, \mathbf{L}_r\boldsymbol{\eta}\rangle = \langle \boldsymbol{\eta}, \mathbf{S}_r\boldsymbol{\eta}\rangle, \tag{8}$$

where $\mathbf{S}_r$ denotes the symmetric part of the matrix $\mathbf{L}_r$, i.e.,

$$\mathbf{S}_r := \tfrac{1}{2}[\mathbf{L}_r + \mathbf{L}_r^{\dagger}]. \tag{9}$$

The eigenvalues $\lambda_1 \geqslant \lambda_2 \geqslant \cdots \geqslant \lambda_r$ of the symmetric tensor $\mathbf{S}_r \in \mathbb{R}^{r\times r}$, therefore, measure the instantaneous linear growth (or decay) of perturbations within the OTD subspace $E_r(t)$. Furthermore, the identity (8) implies the inequality

$$|\boldsymbol{\eta}(t_0)|e^{\lambda_{\min}(t-t_0)} \leqslant |\boldsymbol{\eta}(t)| \leqslant |\boldsymbol{\eta}(t_0)|e^{\lambda_{\max}(t-t_0)}, \quad \forall\, t \in [t_0, t_0 + T], \tag{10}$$

for $T > 0$ and $\lambda_{\min} \leqslant \lambda_{\max}$ defined as

$$\lambda_{\min} := \min_{\tau\in[t_0,t_0+T]} \lambda_r(\tau), \quad \lambda_{\max} := \max_{\tau\in[t_0,t_0+T]} \lambda_1(\tau). \tag{11}$$

In particular, if $\lambda_{\min}$ is positive, the perturbations within the OTD subspace $E_r(t_0)$ grow exponentially fast over the time interval $[t_0, t]$.

Based on the above observation, we use the eigenvalue configuration of the symmetric tensor $\mathbf{S}_r$ as the indicator for an upcoming burst. In so doing, we assume that, after the initial transients, the OTD modes capture the most unstable flow-invariant subspace along a time-dependent trajectory. As pointed out in Sec. II B, this has been proved by Babaee and Sapsis [29, Theorem 2.3] for hyperbolic fixed points, but remains an open problem for time-dependent trajectories.

In case the slow manifold is known as a graph over the slow variables, the connection between the largest eigenvalue λ_1 of the reduced symmetric tensor $\mathbf{S}_r$ and the instabilities transverse to the slow manifold can be made rigorous as shown by Haller and Sapsis [33]. In practice, this graph is rarely known.

III. CONCEPTUAL MODEL

For illustrative purposes, we construct a prototype system which has simple dynamics with bursting episodes. The system is described by the set of nonlinear ODEs,

$$\begin{aligned} \dot{x} &= \alpha x + \omega y + \alpha x^2 + 2\omega xy + z^2, \\ \dot{y} &= -\omega x + \alpha y - \omega x^2 + 2\alpha xy, \\ \dot{z} &= -\lambda z - (\lambda + \beta)xz, \end{aligned} \tag{12}$$

where $\alpha, \omega, \lambda, \beta > 0$ are constant parameters. We define $\mathbf{u} = (x, y, z)$ and denote the right-hand side of (12) by $\mathbf{F}(\mathbf{u})$. The plane $z = 0$ is an invariant manifold containing the two fixed points

$$\mathbf{u}_1 = (0,0,0), \quad \mathbf{u}_2 = (-1,0,0).$$

Linearizing around these fixed points, we obtain

$$\begin{aligned} \nabla\mathbf{F}(\mathbf{u}_1) &= \begin{pmatrix} \alpha & \omega & 0 \\ -\omega & \alpha & 0 \\ 0 & 0 & -\lambda \end{pmatrix}, \\ \nabla\mathbf{F}(\mathbf{u}_2) &= \begin{pmatrix} -\alpha & -\omega & 0 \\ \omega & -\alpha & 0 \\ 0 & 0 & \beta \end{pmatrix}. \end{aligned} \tag{13}$$

The plane $z = 0$ is the linear unstable manifold E^u of $\mathbf{u}_1$ corresponding to the eigenvalues $\alpha \pm i\,\omega$. The plane $z = 0$ is also the linear stable manifold E^s of the fixed point $\mathbf{u}_2$ with eigenvalues $-\alpha \pm i\,\omega$. In the following, we set $\alpha = 0.01$, $\omega = 2\pi$, and $\lambda = \beta = 0.1$.

Figure 3 shows a trajectory of the system starting near the origin. Perturbations around the fixed point $\mathbf{u}_1$ spiral away from the origin due to the instability in the $z = 0$ plane. Since $z = 0$ is also the stable manifold of the fixed point $\mathbf{u}_2$, the perturbed trajectory is attracted towards $\mathbf{u}_2$. Due to the small stability exponent $\alpha = 0.01$, this process takes place over a long period of time during which the z component of the trajectory stays small. Once close enough to the fixed point $\mathbf{u}_2$, its unstable manifold repels the trajectory away from the $z = 0$ plane, resulting in a rapid growth of the z component. Finally, the trajectory is carried back to the fixed point $\mathbf{u}_1$ along the heteroclinic orbit connecting the two fixed points. The above process repeats once the trajectory is back in the neighborhood of the origin $\mathbf{u}_1$.

Now we investigate the ability of the OTD modes to capture the instability responsible for the bursts. It is clear from the linearization that around the fixed point $\mathbf{u}_1$ the most unstable direction is within the x-y plane. Near fixed point $\mathbf{u}_2$, however, the z direction becomes the most unstable. We solve Eq. (12) together with the OTD equation (4) with a single OTD mode ($r = 1$). We choose the initial conditions $\mathbf{u} = (0, 0.01, 0.01)^{\top}$ and $\mathbf{v}_1(0) = \frac{1}{\sqrt{2}}(1,1,0)^{\top}$.

Figure 4(a) shows the evolution of $\sqrt{v_{1,1}^2 + v_{1,2}^2}$ and $v_{1,3}$, where $v_{1,i}$ denote the components of $\mathbf{v}_1$, i.e., $\mathbf{v}_1 = (v_{1,1}, v_{1,2}, v_{1,3})$. For a long time, while the trajectory is spiraling away from $\mathbf{u}_1$, the z component $v_{1,3}$ remains almost zero. As the trajectory moves towards the fixed point $\mathbf{u}_2$, a sharp transition occurs around time $t = 550$, where the OTD mode $\mathbf{v}_1$ becomes almost orthogonal to the x-y plane and aligns with the z direction. Note that this transition (at $t = 550$) occurs well before the first burst (at $t = 950$) is observed [compare to Fig. 3(b)].

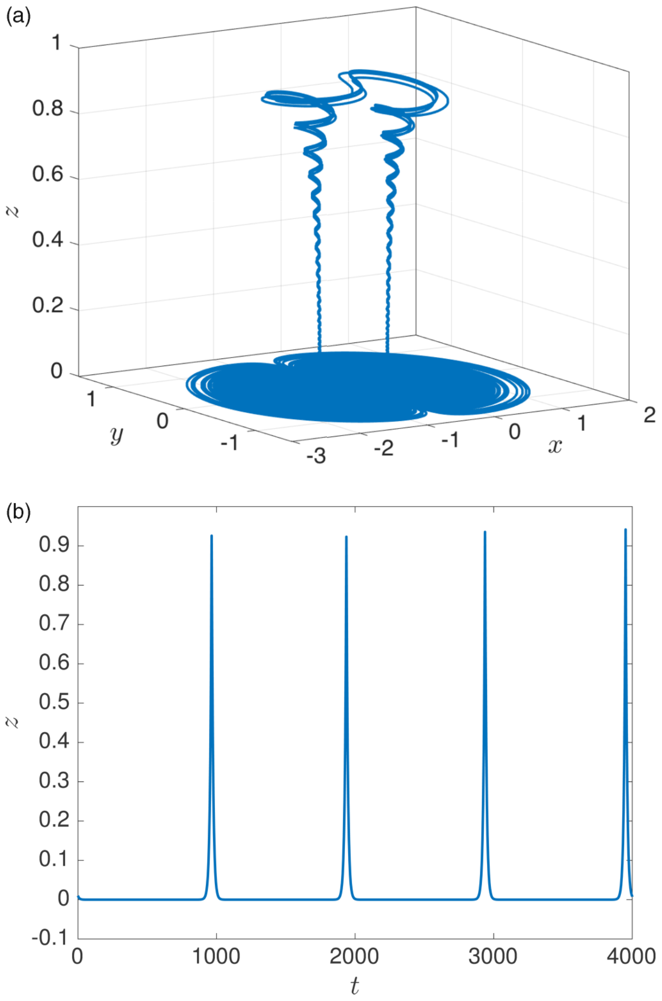

FIG. 3. A trajectory of the system (12) with parameters $\alpha = 0.01$, $\omega = 2\pi$, $\lambda = 0.1$, and $\beta = 0.1$. The initial condition is (0,0.01,0.01). (a) The trajectory $\mathbf{u}(t)$ in the state space. (b) The time series of the z component of the trajectory for 4×10^3 time units.

Figure 4(b) shows the eigenvalue λ_1 of the reduced symmetric matrix $\mathbf{S}_r$ as a function of time. Since we only use one mode, the eigenvalue is trivial: $\lambda_1(t) = \langle \mathbf{v}_1(t), \nabla\mathbf{F}(\mathbf{u}(t))\mathbf{v}_1(t)\rangle$. Over the initial 550 time units, where the OTD mode $\mathbf{v}_1(t)$ is almost parallel to the x-y plane, the eigenvalue λ_1 oscillates rapidly around zero. As a result, any instantaneous growth in the OTD subspace is rapidly counteracted by an instantaneous decay. After time $t = 550$, when the OTD mode reorients orthogonally to the x-y plane, the eigenvalue λ_1 becomes uniformly positive for a long period of time up until the bursting happens. This allows for persistent growth in the OTD subspace which aligns with the z axis in this period [cf. Eq. (10)]. This instability persists up until the burst eventually happens around $t = 960$. After the burst the eigenvalue λ_1 returns to rapid oscillations around zero.

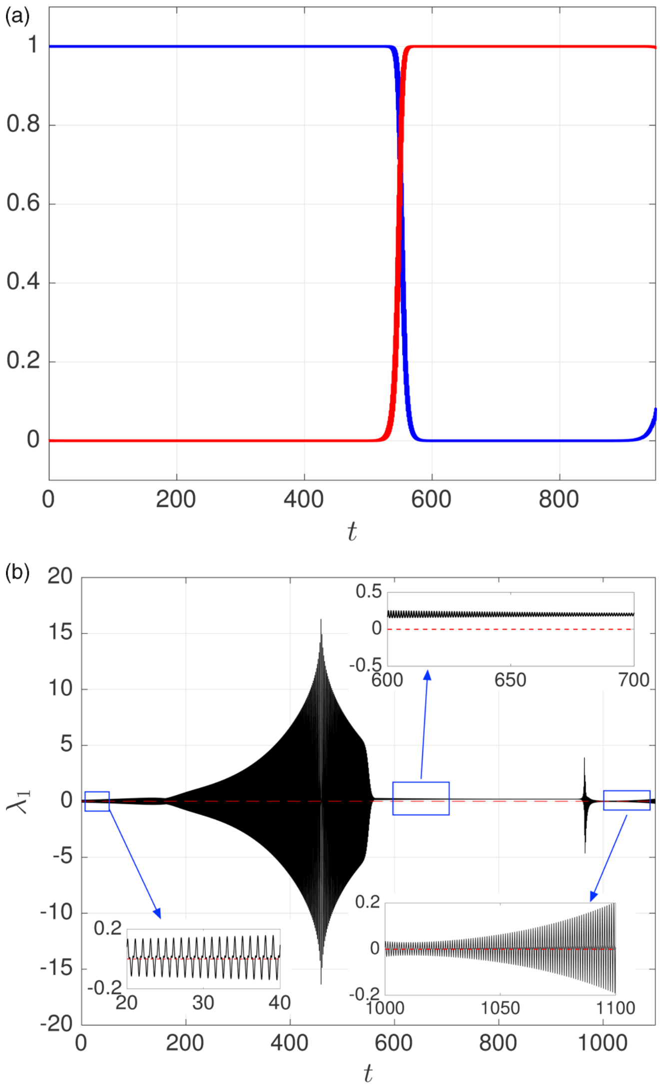

FIG. 4. (a) The evolution of $\sqrt{v_{1,1}^2 + v_{1,2}^2} = \sqrt{1 - v_{1,3}^2}$ (blue) and $v_{1,3}$ (red), where $\mathbf{v}_1 = (v_{1,1}, v_{1,2}, v_{1,3})$. (b) The evolution of the eigenvalue λ_1 as a function of time. The dashed red line marks $\lambda_1 = 0$. Three closeup views are shown in the insets.

IV. TURBULENT FLUID FLOW

A ubiquitous feature of turbulent fluid flow is the intermittent bursts observed in the time series of their measured quantities such as energy dissipation [34,35]. Even at moderate Reynolds numbers, the dimension of the turbulent attractors are high. Best available estimates suggest that the attractor dimension scales almost linearly with the Reynolds number [36–38]. Moreover, no appropriate change of coordinates is available to decompose the system into slow and fast variables [39]. Consequently, intermittencies of turbulent fluid flow are particularly difficult to analyze and hence serve as a challenging example to test our indicator.

A. Governing equations and preliminaries

The two-dimensional Kolmogorov flow is the incompressible Navier–Stokes equations

$$\partial_t \mathbf{u} = -\mathbf{u} \cdot \nabla\mathbf{u} - \nabla p + \nu\Delta\mathbf{u} + \mathbf{f}, \quad \nabla \cdot \mathbf{u} = 0, \tag{14}$$

with the sinusoidal forcing $\mathbf{f} = \sin(ny)\mathbf{e}_1$, where $\mathbf{e}_1 = (1,0)^\top$ and n is a positive integer [40]. The flow is defined on the torus $\mathbf{x} = (x,y) \in \mathbb{T}^2 = [0,2\pi] \times [0,2\pi]$ (i.e., periodic boundary

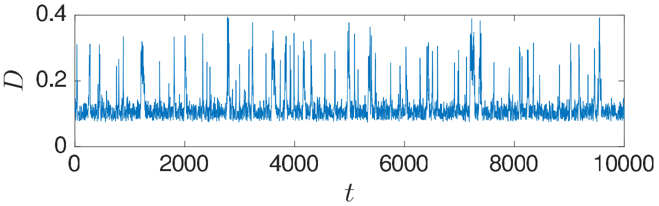

FIG. 5. Evolution of the energy dissipation D along a trajectory of the Kolmogorov flow (14) with $n = 4$ and $\mathrm{Re} = 40$.

conditions). The solution is the time-dependent pair of velocity field $\mathbf{u}(\mathbf{x},t)$ and pressure $p(\mathbf{x},t)$. The nondimensional viscosity ν is the inverse of the Reynolds number, $\nu = 1/\mathrm{Re}$.

The energy E, energy dissipation D, and energy input I of the system are defined as

$$E(t) = \frac{1}{2L^2}\iint_{\mathbb{T}^2} |\mathbf{u}(\mathbf{x},t)|^2 d\mathbf{x}, \quad D(t) = \frac{\nu}{L^2}\iint_{\mathbb{T}^2} |\omega(\mathbf{x},t)|^2, \tag{15}$$
$$I(t) = \frac{1}{L^2}\iint_{\mathbb{T}^2} \mathbf{u}(\mathbf{x},t)\cdot\mathbf{f}(\mathbf{x},t)d\mathbf{x},$$

where $L = 2\pi$ is the size of the domain and ω is the vorticity field. One can show, from the Navier-Stokes equation (14), that these three quantities satisfy $\dot{E} = I - D$ along any trajectory.

The Kolmogorov flow has a *laminar* solution,

$$\mathbf{u}_{\mathrm{lam}} = \frac{\mathrm{Re}}{n^2}\sin(ny)\mathbf{e}_1, \tag{16}$$

which is asymptotically stable for forcing wave number $n = 1$ and any Reynolds number Re [41,42]. For $n > 1$ and sufficiently high Re, however, the laminar solution is unstable. Moreover, numerical evidence suggests that, for high-enough Reynolds number and $n > 1$, the Kolmogorov flow is chaotic [40,43]. Figure 5, for instance, shows the evolution of the energy dissipation measured along a trajectory of the Kolmogorov flow with $n = 4$ and $\mathrm{Re} = 40$. The energy dissipation mostly oscillates irregularly around $D = 0.1$ and never settles down to a regular pattern. More interestingly, the energy dissipation exhibits intermittent, short-lived episodes of higher energy dissipation that we wish to predict.

B. OTD modes for the Kolmogorov flow

In Sec. II B, we introduced the OTD modes for ordinary differential equations. The OTD modes for partial differential equations (PDEs) are defined in a similar manner, although more care should be exercised due to the infinite dimensionality of the system. In analogy with the ODEs, we define

$$\mathbf{F}(\mathbf{u}) = \mathbb{P}(-\mathbf{u}\cdot\nabla\mathbf{u} + \nu\Delta\mathbf{u} + \mathbf{f}), \tag{17}$$

where $\mathbb{P}$ denotes the projection onto space of divergence-free vector fields, $\nabla\cdot\mathbf{u} = \mathbf{0}$. As opposed to the ODEs, where $\mathbf{F}$ is a vector field, here it is a nonlinear differential operator acting on functions $\mathbf{u} : \mathbb{T}^2 \times \mathbb{R} \to \mathbb{R}^2$ that are sufficiently smooth.

We denote the linearization of $\mathbf{F}$ around the state $\mathbf{u}$ by $\mathbf{L}_{\mathbf{u}}$ whose action on sufficiently smooth functions $\mathbf{v} : \mathbb{T}^2 \times \mathbb{R} \to \mathbb{R}^2$ is given by

$$\mathbf{L}_{\mathbf{u}}\mathbf{v} := \mathbb{P}(-\mathbf{u}\cdot\nabla\mathbf{v} - \mathbf{v}\cdot\nabla\mathbf{u} + \nu\Delta\mathbf{v}). \tag{18}$$

The OTD modes $\{\mathbf{v}_1,\mathbf{v}_2,\ldots,\mathbf{v}_r\}$ then satisfy the set of coupled PDEs

$$\frac{\partial\mathbf{v}_i}{\partial t} = \mathbf{L}_{\mathbf{u}}\mathbf{v}_i - \sum_{j=1}^{r}\langle\mathbf{L}_{\mathbf{u}}\mathbf{v}_i,\mathbf{v}_j\rangle\mathbf{v}_j, \quad i\in\{1,2,\ldots,r\}, \tag{19}$$

where $\langle\cdot,\cdot\rangle$ denotes some appropriate inner product. Here we use the L^2 inner product

$$\langle\mathbf{v},\mathbf{w}\rangle := \iint_{\mathbb{T}^2}\mathbf{v}(\mathbf{x},t)\cdot\mathbf{w}(\mathbf{x},t)d\mathbf{x}. \tag{20}$$

We integrate Eq. (19) with initial conditions

$$\mathbf{v}_k(\mathbf{x},0) = \frac{1}{\pi\sqrt{2}}\begin{pmatrix}\sin(ky)\\ 0\end{pmatrix}, \quad k = 1,2,\ldots,r, \tag{21}$$

which are divergence free and mutually orthogonal and have unit L^2 norm.

The restriction of the infinite-dimensional operator $\mathbf{L}_{\mathbf{u}}$ to the time-dependent OTD subspace $\{\mathbf{v}_k\}_{1\leqslant k\leqslant r}$ is a reduced finite-dimensional linear operator $\mathbf{L}_r$. In the OTD basis, the reduced operator $\mathbf{L}_r$ is given by the $r\times r$ matrix whose entries are given by

$$[\mathbf{L}_r]_{ij} = \langle\mathbf{v}_i,\mathbf{L}_{\mathbf{u}}\mathbf{v}_j\rangle, \quad i,j\in\{1,2,\ldots,r\}. \tag{22}$$

Although the linear operator (18) acts on an infinite-dimensional function space, the reduced operator $\mathbf{L}_r$ is a finite-dimensional linear map whose symmetric part $\mathbf{S}_r$ is defined by (9).

We numerically integrate the Kolmogorov equation (14) and its associated OTD equations (19). To evaluate the right-hand sides of the equations, we use a standard pseudospectral scheme with 2/3 dealiasing [44]. Unless stated otherwise, 128×128 Fourier modes are used for the simulations reported below. For the time integration, we use the Runge-Kutta scheme RK5(4) of Dormand and Prince [45] with relative and absolute error tolerances set to 10^{-5}.

C. Asymptotically stable regime

As mentioned earlier, for the forcing wave number $n = 1$, the laminar solution (16) of the Kolmogorov equation (14) is asymptotically stable at any Re number. Moreover, the laminar solution is also the global attractor [42]. This regime is not our primary interest. It, however, does help illustrate the evolution of the OTD modes in an unambiguous setting.

We numerically solve the Kolmogorov equation and its associated OTD equations with $r = 2$. The state $\mathbf{u}$ is initially random in phase with an exponentially decaying energy spectrum. The initial conditions for the OTD modes are given in (21). Figure 6 shows the initial condition and the evolution of the state $\mathbf{u}$ and the OTD modes $\mathbf{v}_1$ and $\mathbf{v}_2$ at select time instances.

The eigenvalues of the symmetric tensor $\mathbf{S}_2$ are shown in Fig. 7. As the flow evolves towards the laminar solution, the eigenvalues of $\mathbf{S}_2$ oscillate before they converge to their asymptotic value of -0.025. One of the eigenvalues assumes positive values during this transition, signaling perturbations that can instantaneously grow. Since the laminar solution is the global attractor, the instantaneous growth cannot be sustained and decays eventually. As the state $\mathbf{u}(t)$ converges

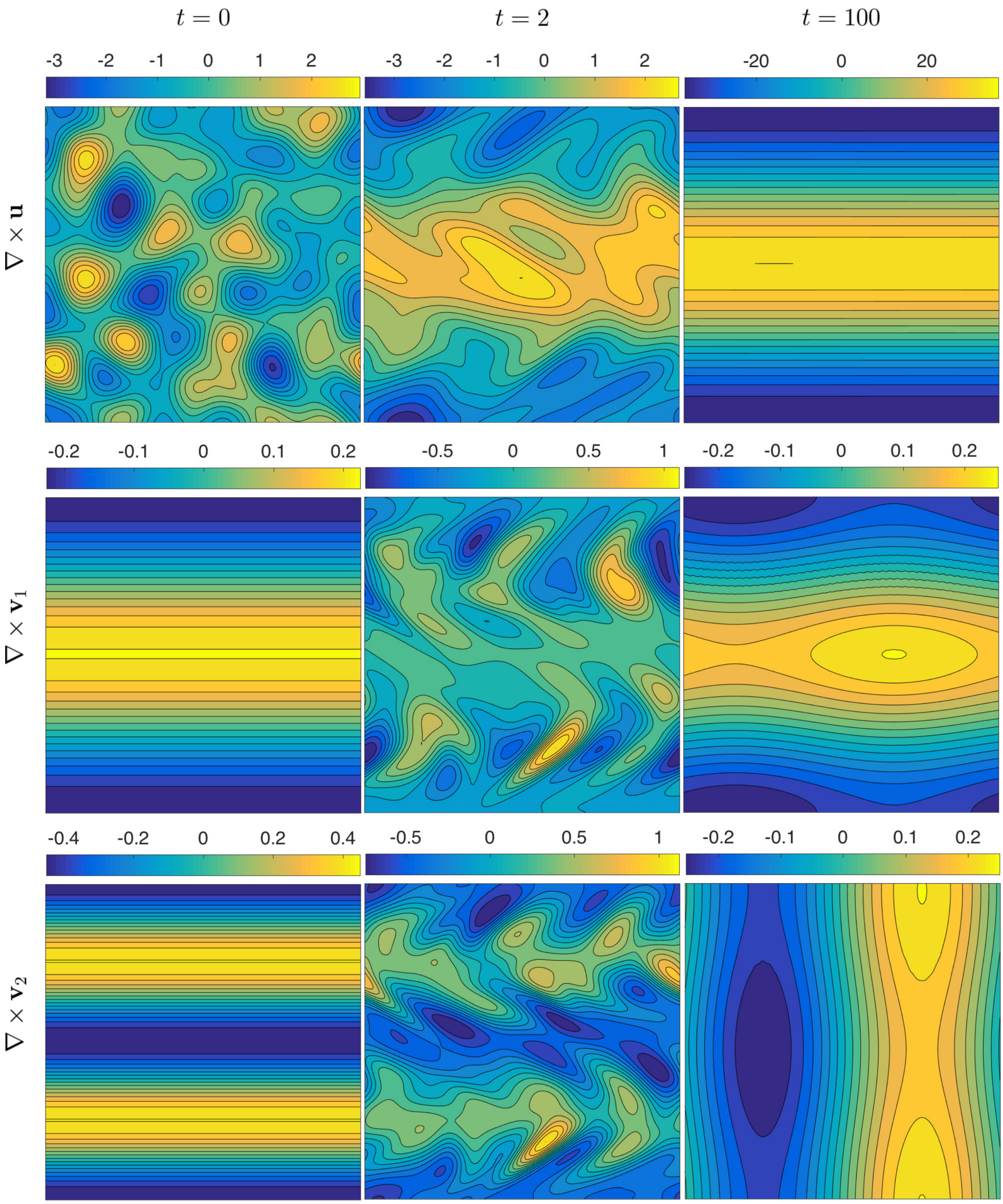

FIG. 6. The Kolmogorov flow in the asymptotically stable regime with $n = 1$ and Re $= 40$. (Top row) The vorticity field at times $t = 0$, 2, and 100. (Middle row) Curl of the first OTD mode $\mathbf{v}_1$ at $t = 0$, 2, and 100. (Bottom row) Curl of the second OTD mode $\mathbf{v}_2$ at $t = 0$, 2, and 100. The colors correspond to the only nonzero component of the curls. All panels show the entire domain $[0,2\pi] \times [0,2\pi]$.

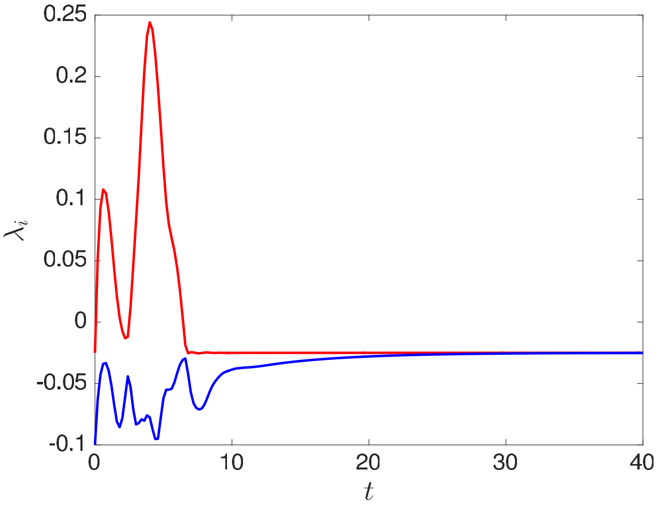

FIG. 7. Eigenvalues of the symmetric matrix $\mathbf{S}_2$ along a trajectory of the Kolmogorov flow in the asymptotically stable regime: $n = 1$ and Re $= 40$.

to the laminar solution (16), the OTD modes $\mathbf{v}_1$ and $\mathbf{v}_2$ converge to the least-stable eigenspace of the linear operator (18) corresponding to eigenvalue -0.025, whose algebraic and geometric multiplicities happen to be equal to 2.

D. Chaotic regime

We turn now to a set of parameters for which the Kolmogorov flow is chaotic. Numerical evidence suggests that, for $n = 4$ and Re $= 40$, the Kolmogorov flow has a strange attractor [43]. More importantly, the energy dissipation D exhibits an intermittent behavior along the trajectories on the strange attractor (see Fig. 5).

Figure 8 shows the energy input I versus the energy dissipation D for a long turbulent trajectory. During the evolution, the energy input and dissipation assume smaller values and are very close to each other sitting near the diagonal. The Kolmogorov flow is driven by the external forcing $\mathbf{f}$ such that growth in the energy input I corresponds to the alignment of the velocity field $\mathbf{u}$ and the forcing [see Eq. (15)]. This alignment leads to an abrupt increase in the energy input I. Consequently, the energy dissipation also increases, bringing the trajectory back to the statistically stationary background.

Based on this observation, one may argue that the growth of the perturbations aligning with the forcing should signal an upcoming burst in the energy input (and consequently the energy dissipation). The instantaneous growth of such a perturbation is measured by $\langle \mathbf{f}, \mathbf{L}_\mathbf{u}\mathbf{f}\rangle$ [cf. Eq. (8)]. For any divergence-free velocity field $\mathbf{u}(t)$ with zero mean, however, a straightforward calculation yields $\langle \mathbf{f}, \mathbf{L}_\mathbf{u}\mathbf{f}\rangle \simeq -7.896$. This seemingly paradoxical result is the consequence of the fact that the forcing $\mathbf{f}$ is not a flow-invariant subspace and, as such, the instantaneously negative value of $\langle \mathbf{f}, \mathbf{L}_\mathbf{u}\mathbf{f}\rangle$ does not imply decay over finite time intervals. The OTD subspaces, in contrast, are flow invariant and therefore a projection onto them is dynamically meaningful.

The evolution of the eigenvalues of the symmetric tensor $\mathbf{S}_{12}$ along a turbulent trajectory are shown in Fig. 9. The first

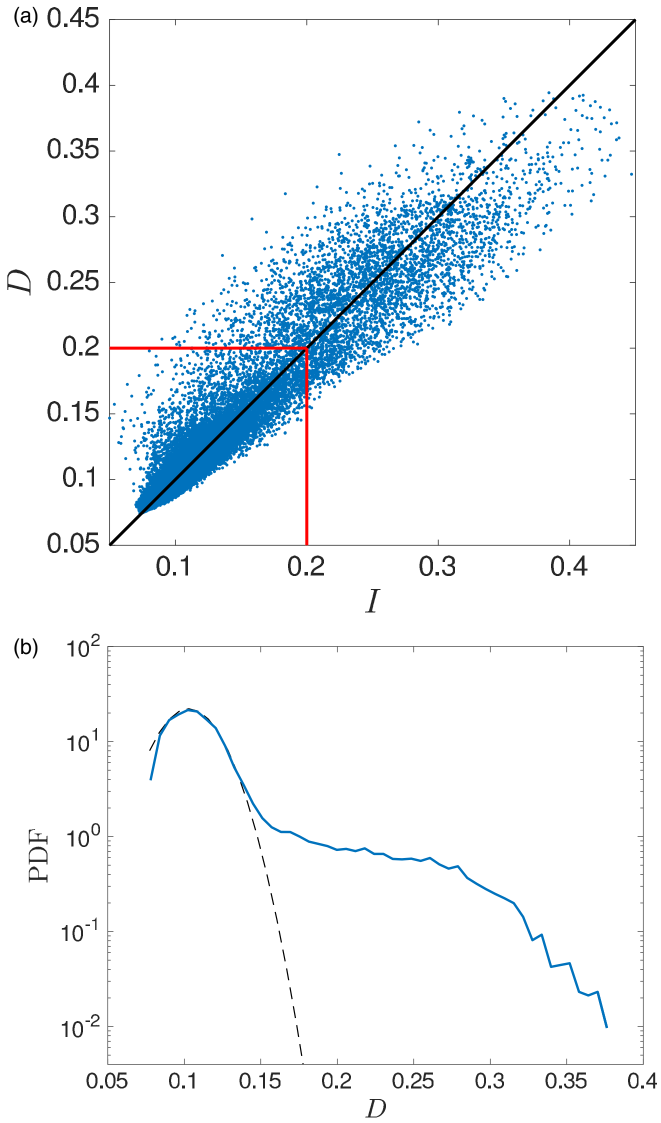

FIG. 8. (a) Energy input I versus energy dissipation D shown for a long turbulent trajectory. The dots correspond to 5×10^4 time instances each 0.2 time units apart. The trajectory spends approximately 91.8% of its lifetime inside the red box. The black line is the diagonal $I = D$. (b) The probability density function (PDF) of the energy dissipation. The dashed black line marks the PDF of a Gaussian distribution with mean 0.103 and standard deviation 0.018.

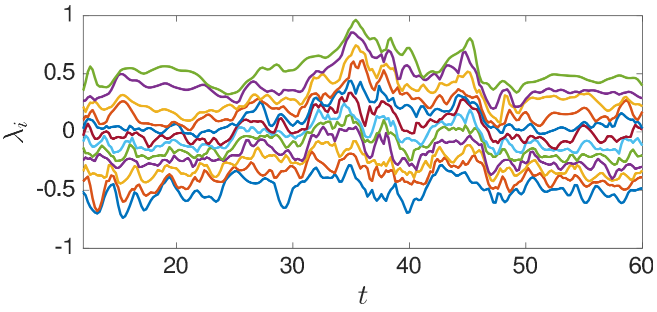

FIG. 9. Evolution of the eigenvalues $\lambda_1 \geqslant \lambda_2 \geqslant \cdots \geqslant \lambda_{12}$ of the reduced symmetric tensor $\mathbf{S}_{12}$ along a chaotic trajectory of the Kolmogorov flow.

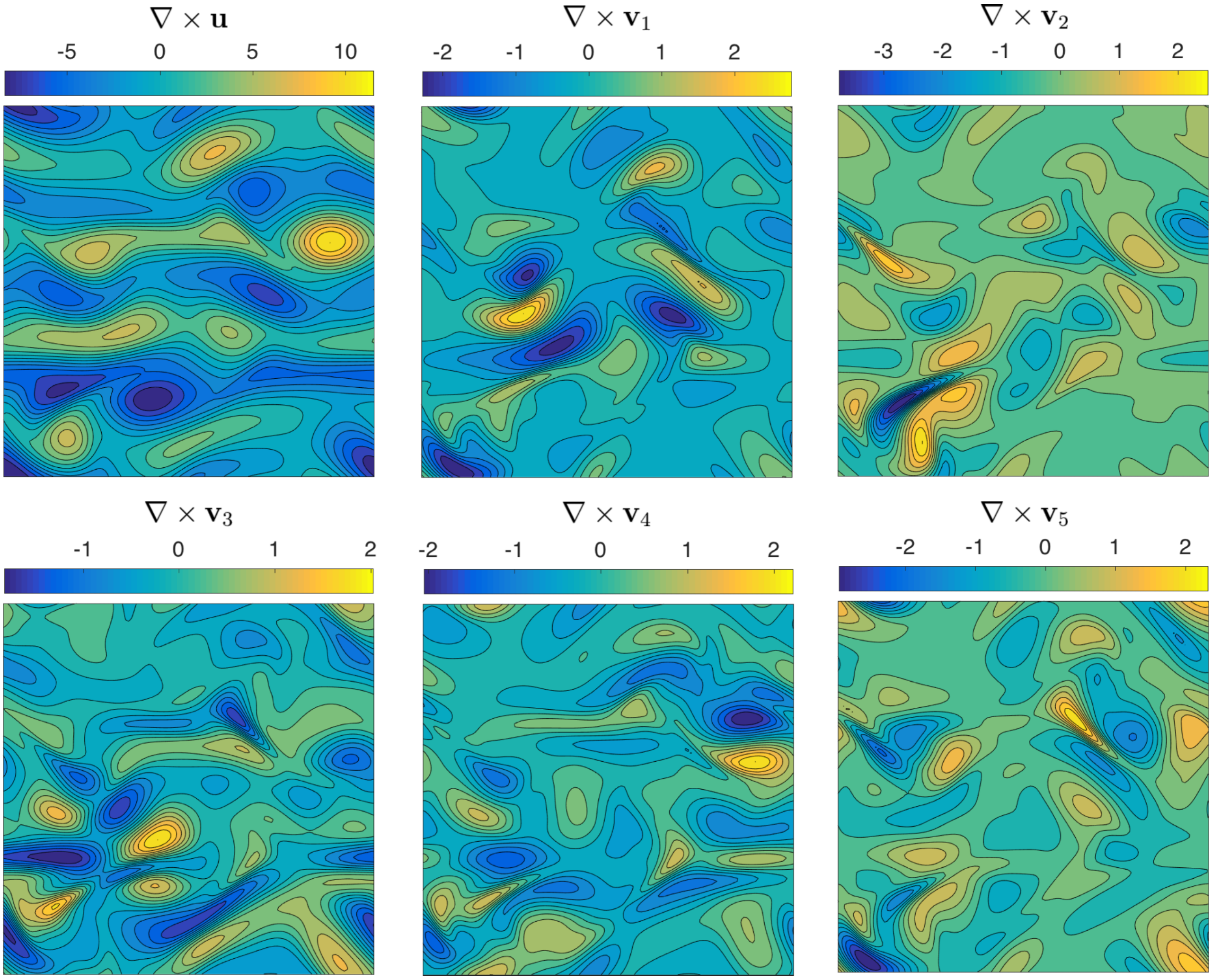

FIG. 10. Snapshots of the curl of $\mathbf{u}$, $\mathbf{v}_1$, $\mathbf{v}_2$, $\mathbf{v}_3$, $\mathbf{v}_4$, and $\mathbf{v}_5$ (from top left to bottom right, respectively) at time $t = 34.6$. The colors correspond to the only nonzero component of the curls. All panels show the entire domain $[0,2\pi] \times [0,2\pi]$.

four eigenvalues are positive for all t in this time window, signaling the very unstable nature of the flow.

Figure 10 shows select OTD modes at time $t = 34.6$ right before a burst in the energy dissipation occurs. The modes themselves do not exhibit a distinguished structural feature that could suggest an immediate connection to the burst. We notice, however, that the largest eigenvalue λ_1 of the symmetric part of the reduced linear operator $\mathbf{L}_r$ increases significantly just before the bursting (see Fig. 11), while the energy dissipation is within one standard deviation from its mean value at that time. Since the eigenvalue tends to oscillate rapidly and irregularly, mere visual inspection does not yield a satisfactory conclusion. In the next section, we quantify the correlation between the eigenvalue λ_1 and the energy dissipation D through conditional statistics.

These statistics are computed from a large set of numerical simulations that are generated in the following manner. We solve the Kolmogorov equation (14) from 17 separate initial conditions which are random in phase and have exponentially decaying energy spectra. For each of the 17 simulations, we simultaneously solve the coupled OTD equations (19) with the initial conditions (21). The solutions of the Kolmogorov equation and the associated OTD equations are evolved for 1100 time units and saved to the disk every 0.2 time unit. To ensure that the results are not influenced by the initial transients, we discard the data from the first 100 time units of each simulation. The following statistics are computed from the remaining 85 000 saved data points.

E. Conditional statistics

In order to quantify the predictive power of the eigenvalues of reduced symmetric matrix $\mathbf{S}_r$, we use Bayesian statistics [46]. First, for a given scalar quantity $q(t)$, we define

$$\bar{q}(t;t_i,t_f) = \max_{\tau\in[t+t_i,t+t_f]} q(\tau), \tag{23}$$

where $0 < t_i < t_f$ are prescribed numbers. At any time t, the quantity $\bar{q}(t;t_i,t_f)$ equals the maximum value of q over a future time interval $[t+t_i,t+t_f]$. For notational simplicity, we use the shorthand notation $\bar{q}(t)$ for $\bar{q}(t;t_i,t_f)$.

We would like to quantify the predictive power of a given indicator $\alpha(t)$. In particular, we would like to assess whether large peaks of the indicator $\alpha(t)$ at a time t coincide with

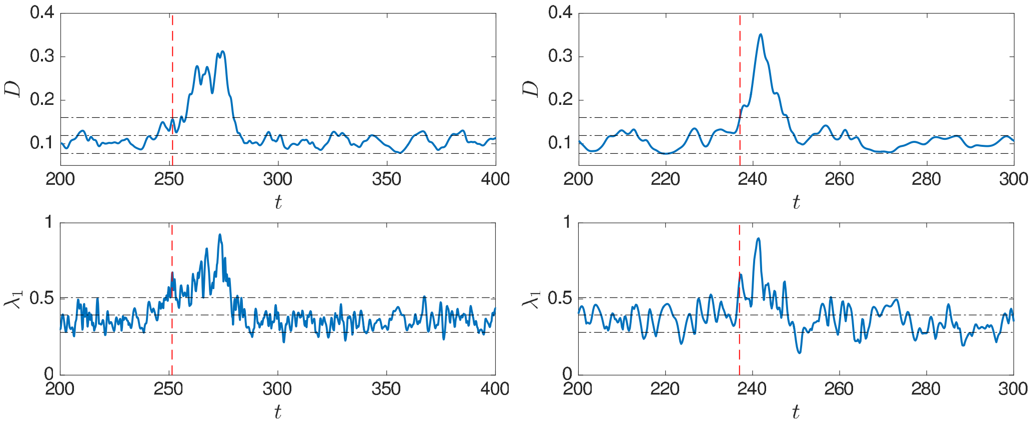

FIG. 11. Evolution of the energy dissipation D and the eigenvalue λ_1 along two different trajectories (each column corresponds to a separate trajectory). The horizontal dashed lines mark the mean, the mean plus one standard deviation and the mean minus one standard deviation of the corresponding quantity.

large values of the observable q over a future time interval $[t + t_i, t + t_f]$.

To this end, we use the joint probability density function (PDF) of $\bar{q}$ and α. The joint PDF of $\bar{q}$ and α is defined as the scalar function $p_{\bar{q},\alpha} : \mathbb{R} \times \mathbb{R} \to \mathbb{R}^+$ that satisfies

$$\mathcal{P}(q_1 \leqslant \bar{q} \leqslant q_2, \alpha_1 \leqslant \alpha \leqslant \alpha_2) = \int_{q_1}^{q_2} \int_{\alpha_1}^{\alpha_2} p_{\bar{q},\alpha}(\bar{q}',\alpha')d\bar{q}'\,d\alpha' \tag{24}$$

for all $q_1, q_2, \alpha_1, \alpha_2 \in \mathbb{R}$, where $\mathcal{P}$ denotes the probability. The conditional probability density function of $\bar{q}$ (conditioned on α) is then given by

$$p(\bar{q}|\alpha) = \frac{p_{\bar{q},\alpha}(\bar{q},\alpha)}{p_\alpha(\alpha)}, \tag{25}$$

where p_α is the probability density function of the indicator α.

Roughly speaking, $p(\bar{q}(t) = \bar{q}_0 | \alpha(t) = \alpha_0)$ denotes the likelihood of the maximum of the scalar q over the time interval $[t + t_i, t + t_f]$ being q_0 given that the value of α at time t is α_0. More precisely, the conditional probability of $\bar{q}$ over the time interval $[t + t_i, t + t_f]$ being greater than a prescribed value q_0 is given by

$$\begin{aligned}\mathcal{P}(\bar{q}(t) > q_0 | \alpha(t) = \alpha_0) &= \mathcal{P}\left\{ \max_{\tau \in [t+t_i, t+t_f]} q(\tau) \geqslant q_0 | \alpha(t) = \alpha_0 \right\} \\ &= \int_{q_0}^{\infty} p(\bar{q}'|\alpha_0)d\bar{q}'.\end{aligned} \tag{26}$$

In particular, if an extreme event corresponds to values of q greater than a prescribed critical value q_c, the probability of the extreme event taking place over the time interval $[t + t_i, t + t_f]$, given that $\alpha(t) = \alpha_0$, is measured by

$$\begin{aligned}P_{EE}(\alpha_0) := \mathcal{P}\left\{ \max_{\tau \in [t+t_i, t+t_f]} q(\tau) \geqslant q_c | \alpha(t) = \alpha_0 \right\} \\ = \int_{q_c}^{\infty} p(\bar{q}'|\alpha_0)d\bar{q}',\end{aligned} \tag{27}$$

where P_{EE} denotes the probability of an extreme event taking place over the future time interval $[t + t_i, t + t_f]$.

In the case of the Kolmogorov flow, the observed quantity q is the energy dissipation D and the indicator α is the largest eigenvalue λ_1 of the reduced symmetric tensor $\mathbf{S}_r$ [see Eq. (9)]. The value of the eigenvalue $\lambda_1(t)$ depends on the subspace dimension r. Properties 1 and 2 of the OTD modes listed in Sec. II B imply that λ_1 is an increasing function of the subspace dimension r. We have observed, however, that this eigenvalue eventually approaches an upper envelope for large r (see Fig. 12). For the Kolmogorov flow at $\mathrm{Re} = 40$, the eigenvalues λ_1 with $r \geqslant 8$ are virtually indistinguishable from each other. Based on this observation, we use $r = 8$ in the following analysis.

The joint PDF $p_{\bar{D},\lambda_i}$ and the PDF p_{λ_i} are approximated from a large set of numerical simulations containing roughly 85 000 data points. The conditional PDF $p(\bar{D}|\lambda_i)$ then is computed through the Bayesian relation (25). Figure 13 shows the resulting conditional PDF $p(\bar{D}|\lambda_i)$ for the three largest eigenvalues of $\mathbf{S}_r$. As the three conditional PDFs are qualitatively similar, we only discuss the one corresponding to the largest eigenvalue λ_1.

The conditional PDF exhibits a "bimodal" structure. For $0 < \lambda_1(t) < 0.55$, the maximal future value of the energy dissipation $\max_{\tau \in [t+t_i, t+t_f]} D(\tau)$ is most likely to lie between 0 and 0.15 [the lower left dark region in Fig. 13(a)]. A sharp transition is observed for $0.55 < \lambda_1(t)$ such that for this range of the eigenvalue λ_1, the energy dissipation is more likely to assume values larger that 0.15 over the future time interval $[t + t_i, t + t_f]$.

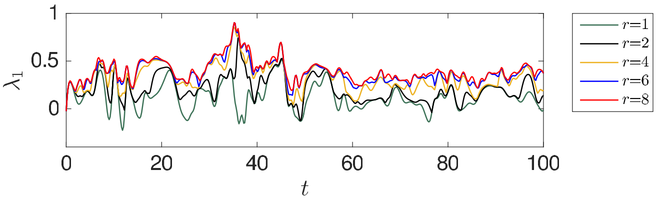

FIG. 12. The largest eigenvalue λ_1 of $\mathbf{S}_r$ as a function of time t for five different values of the subspace dimension r and the Kolmogorov flow at $\mathrm{Re} = 40$. The eigenvalue λ_1 increases with r, eventually converging to an upper envelope.

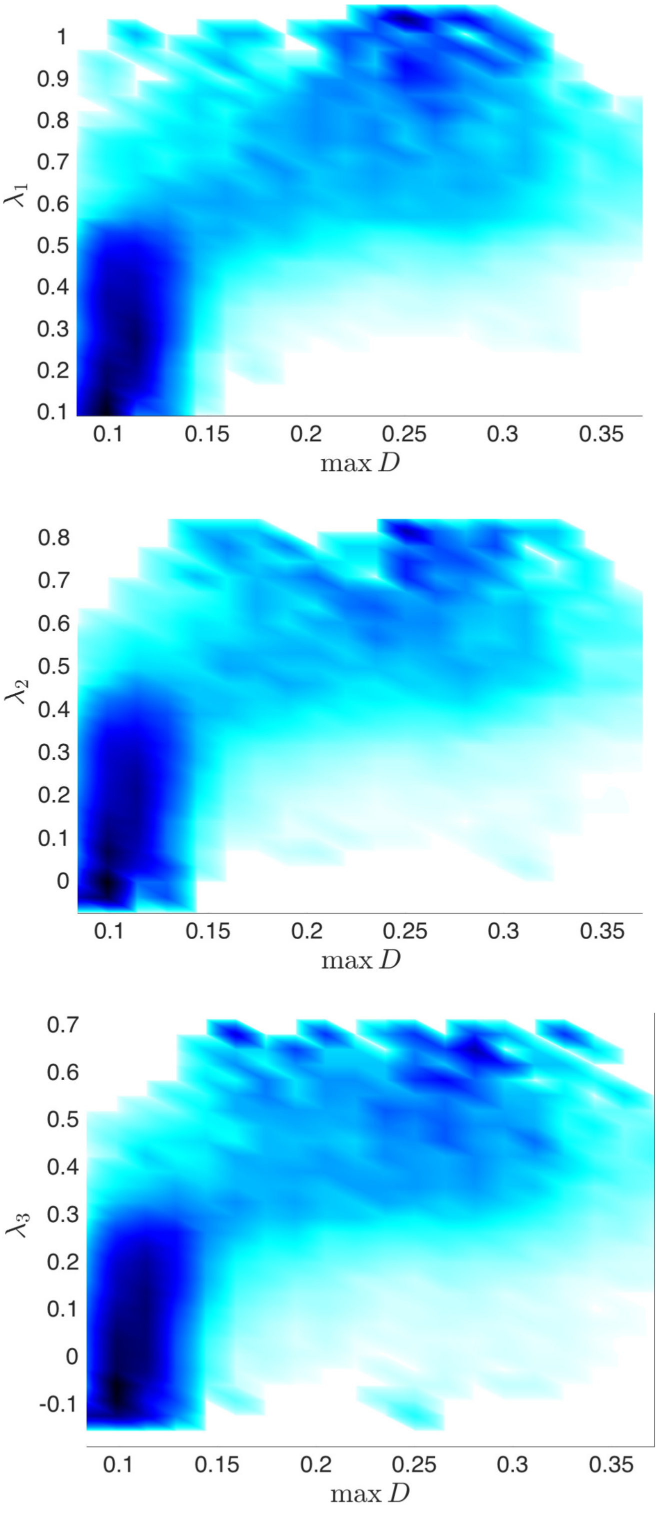

FIG. 13. Conditional PDF of the first three eigenvalues of $\mathbf{S}_8$ and the maximal dissipation $\max_\tau D$, where the maximum is taken over $\tau \in [t + t_i, t + t_f]$, with $t_i = 3$ and $t_f = 5$.

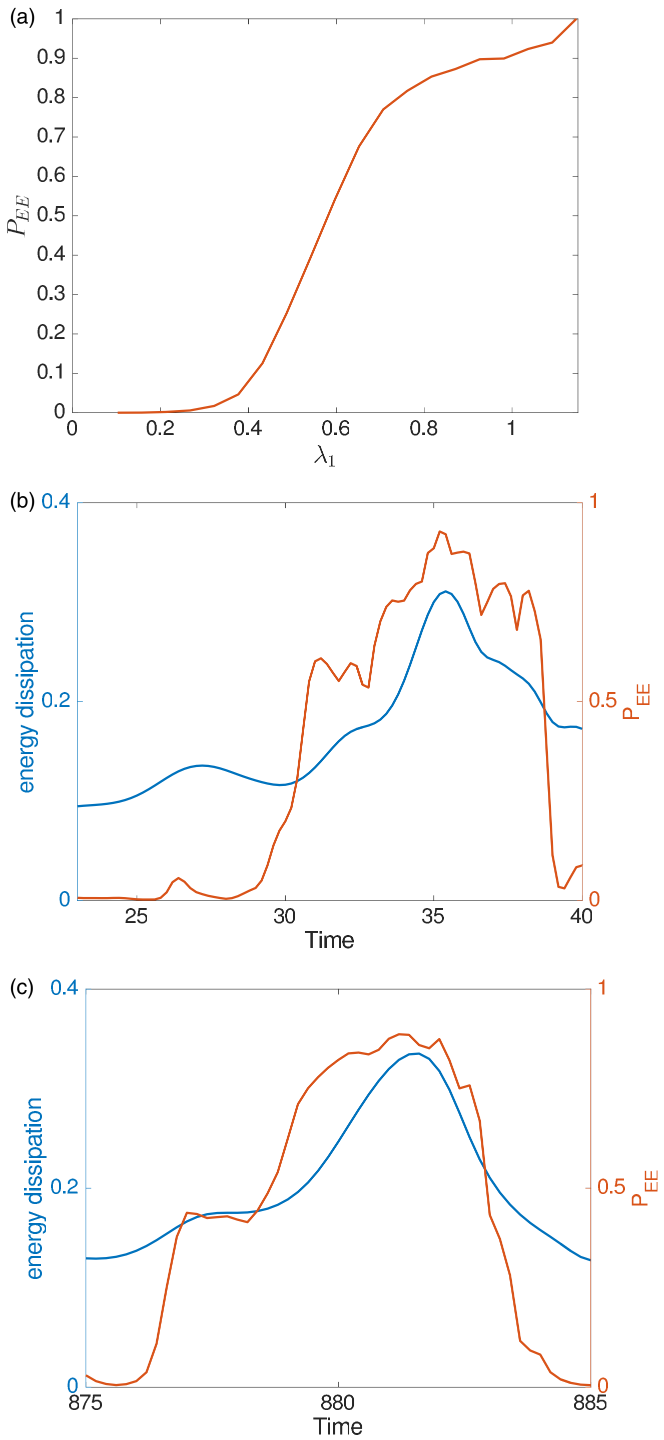

FIG. 14. (a) Probability of the extreme energy dissipation P_{EE} as a function of the value of the indicator λ_1. The probability P_{EE} is computed from the definition (27) with $t_i = 3$ and $t_f = 5$. (b),(c) Close-up view of two episodes of extreme energy dissipation and their corresponding probabilities P_{EE}.

Using this conditional PDF, we compute the probability of extreme events P_{EE} from Eq. (27). From the time series presented in Fig. 5, it is reasonable to associate a burst with values of the energy dissipation larger than 0.2. We use this value as the critical energy dissipation (i.e., $D_c = 0.2$) above which an extreme event is recorded. The resulting probability function is plotted in Fig. 14(a). If at a time instant t the value of λ_1 is smaller than 0.4, the probability of $D(\tau) > D_c$ over the future time interval $\tau \in [t + t_i, t + t_f]$ is virtually zero. For larger values of λ_1, the probability of an extreme event increases monotonically. At $\lambda_1 = 0.55$, the probability of an upcoming extreme event is greater than 50%. Eventually, this probability grows to above 80% at $\lambda_1 \simeq 0.8$.

Using the computed probability of extreme event P_{EE}, we predict, at every given time t, the probability that an extreme event takes place over the future time interval $[t + t_i, t + t_f]$. Figure 14 [panels (b) and (c)], shows two select time windows over which an extreme event occurs. Away from the extreme event, the probability P_{EE} is very low. Just before the extreme event, this probability grows, predicting the upcoming extreme events at least $t_i = 3$ time units in advance.

The parameters $t_i = 3$ and $t_f = 5$ for the time window $[t + t_i, t + t_f]$ are chosen so that the resulting probability of extreme events P_{EE} is an increasing function of the indicator λ_1 and eventually attains the value 1 for large λ_1. This ensures that larger values of the indicator do signal a higher probability of an upcoming extreme event over the future time window $[t + t_i, t + t_f]$. Furthermore, the largest values of the indicator (corresponding to $P_{EE} = 1$) indicate that an extreme event will almost surely take place over the future time window $[t + t_i, t + t_f]$. We have observed that this monotonic property of P_{EE} holds for small t_i. Increasing t_i incrementally, the monotonicity of P_{EE} is eventually lost at $t_i = 3.6$, indicating the upper limit on the predictability horizon of our indicator. The predictability horizon $t_i = 3.6$ is approximately one-third of the decorrelation time of the energy dissipation D. We also find that the results are insensitive to the length of the time window $t_f - t_i$. The results in Figs. 13 and 14 are reported for $t_f - t_i = 2$ to ensure that each time interval $[t + t_i, t + t_f]$ contains, at most, one rare event.

While the above results are reported at Re = 40, we point out that similar conclusions hold at higher Reynolds numbers. Figure 15, for instance, shows the conditional PDF and the probability of extreme events at Re = 100. To fully resolve the flow, the higher resolution of 256 × 256 Fourier modes are used at this Re number. On the other hand, to keep the computational cost reasonable, the linearized operator is reduced to four OTD modes, i.e., $r = 4$.

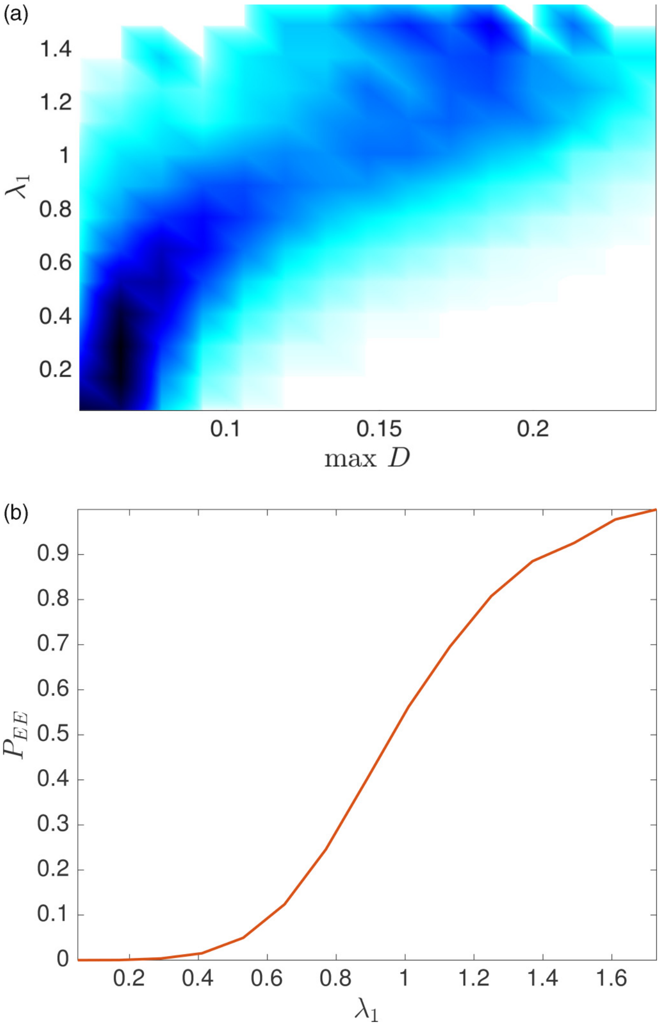

FIG. 15. Conditional PDF (a) and the probability of upcoming extreme energy dissipation (b) for Reynolds number Re = 100.

F. Comparison with dynamic mode decomposition

We carry out a comparison in this section to highlight that the correct choice of the modes to which the linear operator $\mathbf{L_u}$ is reduced is essential. To this end, we repeat the analysis of Sec. IV E, but this time we reduce the operator $\mathbf{L_u}$ to the modes obtained from dynamic mode decomposition (DMD). DMD was proposed by Schmid [47] for extracting a linear approximation to the flow map of a nonlinear dynamical system. The resulting *dynamic modes* (or DMD modes) have proven insightful in the analysis of fluid flows [48,49] and shown to have intricate connections to the invariants of the Koopman operator along time-periodic orbits of the nonlinear system [50,51].

Since the DMD modes are not flow invariant (see Definition 1), the reduction of the linear operator $\mathbf{L_u}$ to these modes is not dynamically meaningful. As a result, the eigenvalues of the symmetric tensor reduced to DMD modes are not expected to reflect the true growth (or decay) of perturbations. To illustrate this, we use the algorithm introduced by Schmid [47] to compute DMD modes from 500 sequential snapshots of the Kolmogorov flow, each 0.2 time unit apart. Next we restrict the operator $\mathbf{L_u}$ to the eight most dominant DMD modes and compute the largest eigenvalue of its symmetric part along all previously computed turbulent trajectories $\mathbf{u}(t)$. The resulting conditional PDF is shown in Fig. 16. As opposed to the OTD modes (cf. Fig. 13), the extreme episodes of the energy dissipation do not show a signature in the DMD-reduced operator.

V. SPATIALLY LOCALIZED EXTREME EVENTS

The energy dissipation in turbulent flows, as discussed in Sec. IV, is a global feature of the state. In spatiotemporal chaos, however, local rare extreme events, in the form of spatially localized structures, are possible. A famous example of such localized extreme events is the ocean rogue waves. Such localized phenomena cannot be quantified from global quantities such as the eigenvalues of the linear operator.

In this section, we illustrate that localized features of the OTD modes can still be of significance for the analysis of spatially localized extreme events. To illustrate this, we consider the modified nonlinear Schrödinger (MNLS) equation which is an approximation to the evolution of sea

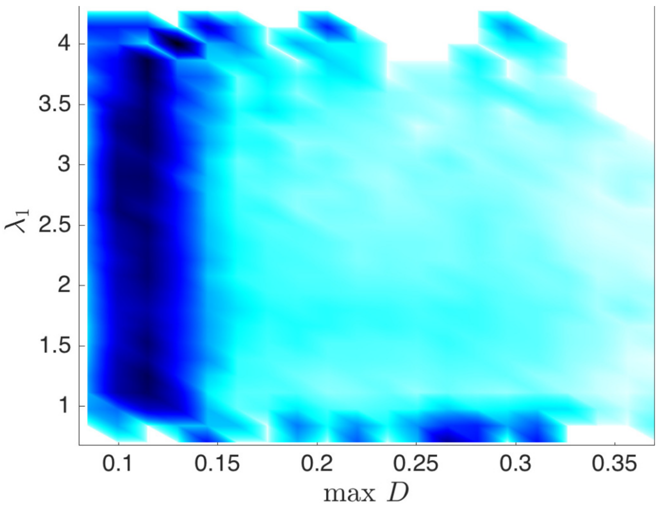

FIG. 16. Same as Fig. 13(a) but now the linear operator is reduced to the eight most dominant DMD modes.

surface elevation in deep waters [52]. The MNLS equation is a higher-order perturbative approximation compared to the nonlinear Schrödinger equation derived by Zakharov [53].

A. MNLS equation

For a complex valued function $u(x,t)$, the MNLS equation (in dimensionless variables) reads

$$\partial_t u = F(u), \tag{28}$$

with

$$F(u) = -\frac{1}{2}\partial_x u - \frac{i}{8}\partial_x^2 u + \frac{1}{16}\partial_x^3 u - \frac{i}{2}|u|^2 u - \frac{3}{2}|u|^2\partial_x u \\ - \frac{1}{4}u^2\partial_x u^* - i\,u\Phi(u), \tag{29}$$

where $i = \sqrt{-1}$, $x \in [0,L]$, and $u(x,t) \in \mathbb{C}$. The asterisk sign denotes the complex conjugation. The function Φ is derived from the velocity potential ϕ,

$$\Phi(u) := \partial_x \phi|_{z=0} = -\tfrac{1}{2}\mathcal{F}^{-1}[|k|\mathcal{F}[|u|^2]], \tag{30}$$

where $\mathcal{F}$ denotes the Fourier transform. The modulus $|u(x,t)|$ is the wave envelope for the surface elevation $h(x,t)$. To the leading-order approximation, we have $h(x,t) = \mathrm{Re}[u(x,t)\exp(i(x-t))]$.

We solve the MNLS equation with the initial conditions $u(x,0) = u_0(x)$ with Gaussian energy spectra and random phases. More precisely, the Fourier transform of the initial condition is given by

$$\widehat{u_0}(k) = \sqrt{2\frac{2\pi}{L}N(q_k)e^{i\theta_k}}, \tag{31}$$

where

$$N(q_k) := \frac{\epsilon^2}{\sigma\sqrt{2\pi}}e^{-\frac{q_k^2}{2\sigma^2}}, \tag{32}$$

is a normal distribution, θ_k are random phases uniformly distributed over $[0,2\pi]$ and $q_k = 2\pi k/L$ is the wave number over the periodic domain of length L. There are three free parameters: ϵ, which controls the wave height; σ, which is the standard deviation of the Gaussian distribution and controls the width of the spectrum of the wave; and, finally, L which is the length of the periodic domain, $x \in [0,L]$.

It is well known that the Gaussian wave groups (31) can grow due to the Benjamin-Feir instability [54] to form extreme waves. The Benjamin-Feir index (BFI) $2\sqrt{2}\epsilon/\sigma$ provides an indicator for the probability of the extreme waves taking place. For large-enough BFI, the nonlinear terms dominate, leading to large-amplitude waves [55]. If BFI is too large, however, the extreme waves happen quite often. To realize rare extreme waves, therefore, a moderate BFI value should be used. Following Mohamad *et al.* [56], we use the parameter values $\epsilon = 0.05$, $\sigma = 0.2$, and $L = 256\pi$, resulting in BFI $= 0.71$. This BFI value allows for the formation of extreme waves at a moderate frequency (not too often and not too rare).

We solve the MNLS (29) equation and its associated OTD equation (19) where $\langle\cdot,\cdot\rangle$ now denotes the standard L^2 inner product on complex valued functions,

$$\langle v,w\rangle := \int_0^L v(x)w^*(x)dx. \tag{33}$$

The initial condition for the OTD modes are sinusoidal and are given by

$$v_i(x,0) = \sqrt{\frac{2}{L}}\sin\left(\frac{2\pi i}{L}x\right).$$

The computation of the OTD modes requires the linearization of the operator (29) as outlined in the Appendix.

For the numerical integration of the MNLS equation (and its associated OTD equation), we use a second-order exponential time-differencing scheme [57,58] in time and a pseudospectral scheme for evaluating the spatial derivatives with 2^{11} Fourier modes. For the statistical analysis presented in the next section, we compute 200 MNLS trajectories, each of length 1000 time units, from the initial conditions of the form (31).

B. Extreme waves and the OTD modes

Figure 17 shows a time window over which an extreme wave appears at around $t = 475$ with a wave height of approximately 0.34 [see panel (a)]. Panel (b) shows a snapshot of the wave, 75 time units earlier at $t = 400$. It exhibits a twin wave packet at around $x = 610$. Whether the twin wave packets lead to an extreme wave depends on the energies and the phases of the packets. A simple extrapolation will rule out the possibility of an extreme wave since the wave height has been decaying over the last 50 time units [the red shaded area in Fig. 17(a)].

During this decay period, however, the OTD mode v_1 shows a persistent localized peak at the same location as the twin wave packets. This signals a persistent localized instability that grows to lead to the extreme wave at time $t = 475$ as shown in Fig. 17(c).

As in the case of the Kolmogorov flow, we use Bayesian statistics to quantify the relation between extreme MNLS waves and the localized peaks of the associated OTD modes. Based on the foregoing observation, we use the maximum height of the first OTD mode v_1 as the indicator α. The quantity to be predicted is the maximum height of the MNLS solution

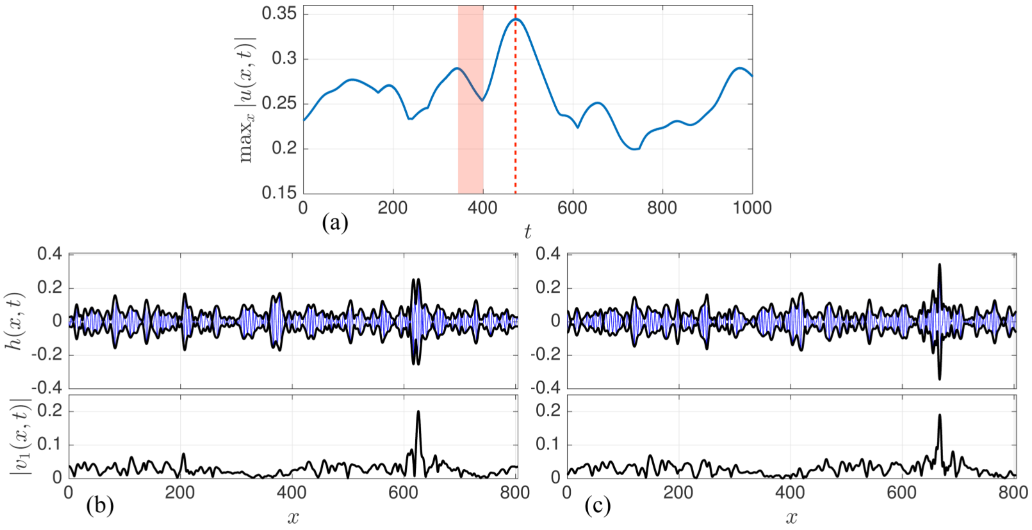

FIG. 17. (a) The spatial maximum of $|u|$ as a function of time t. An extreme event occurs at around $t = 475$, where $\max_x |u| \simeq 0.34$. (b),(c) The surface elevation $h(x,t)$ (blue color) and and the modulus of the OTD mode $|v_1|$ at times $t = 400$ (b) and $t = 475$ (c). The thick black curves in the plots of $h(x,t)$ mark the envelopes $\pm|u(x,t)|$.

u. More precisely,

$$q(t) = \max_{x\in[0,L]} |u(x,t)|, \quad \alpha(t) = \max_{x\in[0,L]} |v_1(x,t)|.$$

The conditional PDF $p(\bar{q}|\alpha)$ is computed as in Sec. IV E. For a given critical wave height h_c, the probability of the rare event is given as in Eq. (27) by

$$P_{EE}(\alpha_0) := \mathcal{P}\left\{ \max_{\tau\in[t+t_i,t+t_f]} \max_{x\in[0,L]} |u(x,\tau)| \geqslant h_c \,\middle|\, \max_{x\in[0,L]} |v_1(x,t)| = \alpha_0 \right\}. \tag{34}$$

Here we set the critical wave height to $h_c = 0.28$, which is approximately the mean plus two standard deviation of the wave heights $\max_x |u|$ for all the computed data. Figure 18(a) shows the resulting conditional PDF $p(\bar{q}|\alpha)$. We observe a strong correlation between the large time-t values of the indicator $\max_x |v_1(x,t)|$ and the large wave heights $|u(x,\tau)|$ over a future time window $\tau \in [t + t_i, t + t_f]$. The forecast skill of the indicator is further demonstrated in Fig. 18(b), showing the probability of an extreme wave P_{EE} as defined in Eq. (34). As in the Kolmogorov flow, the time $t_i = 25$ (approximately four wave periods) is chosen so that the probability function P_{EE} is monotonically increasing, thus ensuring that the high values of the indicator correctly forecast the high probability of an upcoming extreme wave.

VI. SUMMARY AND CONCLUSIONS

We proposed operational indicators for the prediction of rare extreme events (or bursts) in high-dimensional dynamical systems. The motivation for our indicators is based on the observations made about slow-fast systems where the bursts occur along orbits that are transverse and homoclinic to the slow manifold [25–27]. This geometric picture does not lead to an operational method in complex high-dimensional systems where a clear separation between the slow and fast variables is unavailable [28].

We showed that for such systems a signature of bursting can be traced in the eigenvalues of the symmetric part of the linearized dynamics. More precisely, we use the largest eigenvalue λ_1 of the symmetric part of the linearized operator as our indicator. Computing these eigenvalues in high-dimensional systems is computationally expensive. Thanks to the recently introduced notion of OTD modes [29], however, one can reduce the linear operator, in a dynamically consistent fashion, to its most unstable subspace. The reduced operator is low dimensional and its invariants can be readily computed.

We devised a low-dimensional ODE in Sec. III, which has an unambiguous bursting mechanism. For this simple model we showed that the eigenvalue λ_1 becomes uniformly positive several time units before the burst. This allows for instantaneous perturbations within the corresponding subspace to grow. Moreover, the OTD mode aligns with the direction of the growth (i.e., orthogonal to the x-y plane). These together successfully predict the upcoming extreme event.

In the body-forced Navier-Stokes equation considered in Sec. IV, the situation is more complicated as the symmetric part of the reduced operator has several eigenvalues that are positive for all times. The largest eigenvalue λ_1, however, increases significantly before a burst in the energy dissipation takes place. Using Bayesian statistic, we showed that large values of the eigenvalue λ_1 do, in fact, predict upcoming bursts in the energy dissipation. While the results are presented for prediction time $t_i = 3$, they are robust to small variations of this time window. If the prediction time is set too large (larger than $t_i = 3.6$ here), however, the indicator fails to predict the bursts. The predictability time, of course, is problem dependent and is expected to be inversely proportional to the dominant Lyapunov exponent of the system [59].

We also considered extreme waves in a unidirectional model of the nonlinear surface waves in deep ocean. As opposed to the energy dissipation in Navier-Stokes equations, extreme waves are localized in space. Therefore, we do not expect the eigenvalue λ_1 (as a global quantity) to bear significance in their creation. We observe instead that the most unstable OTD

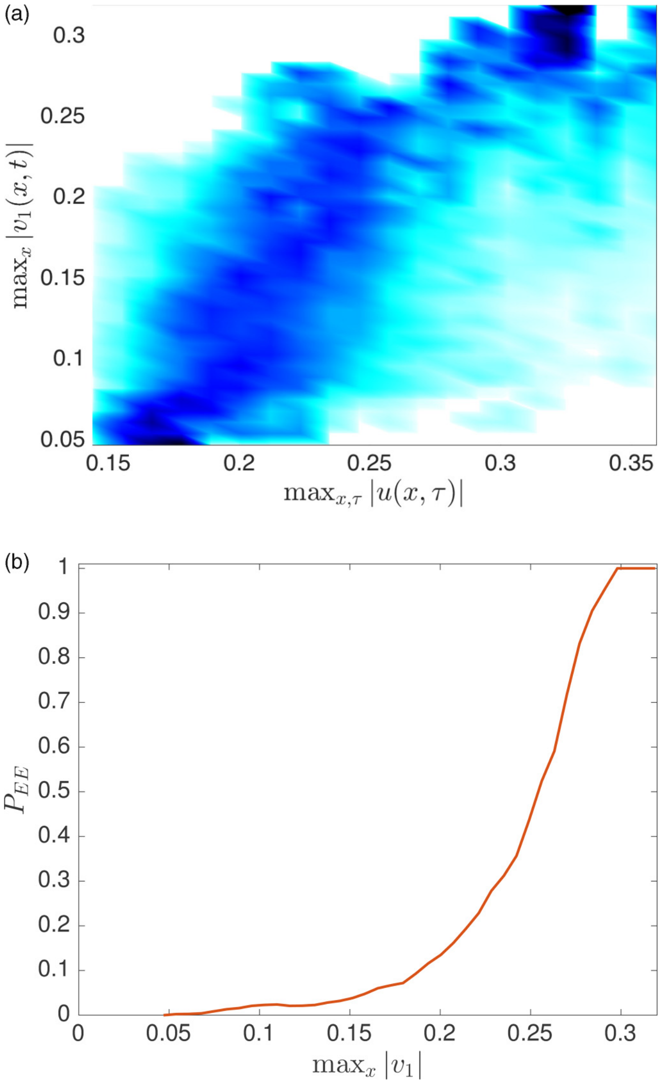

FIG. 18. (a) Conditional PDF for the maximum modulus of the OTD mode v_1 and the solution of the MNLS equation. The maxima are taken over $x \in [0,L]$ and $\tau \in [t+t_i, t+t_f]$, with $t_i = 25$ and $t_f = 26$. (b) The probability of an extreme event P_{EE} computed from the conditional PDF.

mode localizes and grows before an extreme wave appears. The spatial location where the OTD mode localizes is precisely where the extreme wave occurs later in time. This observation indicates a promising direction for space-time prediction of the extreme water waves, complementing the recent work of Cousins and Sapsis [60,61].

We point out that the OTD modes are instrumental to the evaluation of our indicators. This imposes an additional computational cost as the OTD equations need to be solved simultaneously with the governing equations. Moreover, it necessitates that a model of the system is available as a set of differential equations. Therefore, modifying the indicator so that it is applicable to model-independent predictions is highly desirable.

The time-varying nature of the OTD modes distinguishes them from the Lyapunov vectors [62,63] and Oseledec subspaces [64,65] that deal with finite-time or infinite-time instabilities. Yet, the properties discussed in Secs. II B and II C indicate intimate connections with these concepts. A rigorous comparative analysis in this regard will be of interest.

ACKNOWLEDGMENTS

The authors have been supported through the Air Force Office of Scientific Research (Grant No. AFOSR YIP 16RT0548), the Office of Naval Research (Grant No. ONR YIP N00014-15-1-2381), and the National Science Foundation (Grant No. NSF EAGER ECCS 15-1462254).

APPENDIX: THE LINEARIZATION OF THE MNLS EQUATION

We denote the linearization (or Gâteaux differential) of the differential operator F defined in Eq. (29) by $L_u(\cdot)$, which reads

$$\begin{aligned} L_u(v) :=& \lim_{\epsilon\to 0} \frac{F(u+\epsilon v) - F(u)}{\epsilon} \\ =& -\frac{1}{2}\partial_x v - \frac{i}{8}\partial_x^2 v + \frac{1}{16}\partial_x^3 v \\ & - \frac{i}{2}(2|u|^2 v + u^2 v^*) \\ & - \frac{3}{2}(u^* v \partial_x u + u v^* \partial_x u + |u|^2 \partial_x v) \\ & - \frac{1}{4}(2uv\partial_x u^* + u^2 \partial_x v^*) \\ & + \frac{i}{2} u\, \mathcal{F}^{-1}[|k|\, \mathcal{F}[uv^* + vu^*]] \\ & + \frac{i}{2} v\, \mathcal{F}^{-1}[|k| \mathcal{F}(|u|^2)]. \end{aligned} \tag{A1}$$

The only nontrivial calculation above is the last line, corresponding to the linearization of the term $u\Phi(u)$ in (29), which we detail below. First we note that

$$\begin{aligned} &(u+\epsilon v)\Phi(u+\epsilon v) - u\Phi(u) \\ &\quad = \epsilon u\, d\Phi(u;v) + \epsilon v \Phi(u) + O(\epsilon^2), \end{aligned} \tag{A2}$$

where

$$d\Phi(u;v) = \lim_{\epsilon\to 0} \frac{\Phi(u+\epsilon v) - \Phi(u)}{\epsilon}. \tag{A3}$$

From the definition of Φ [see Eq. (30)], we have

$$\begin{aligned} \mathcal{F}[\Phi(u+\epsilon v)] &= -\tfrac{1}{2}|k|\, \mathcal{F}[|u+\epsilon v|^2] \\ &= \mathcal{F}[\Phi(u)] - \epsilon \tfrac{1}{2}|k|\, \mathcal{F}[uv^* + vu^*] + O(\epsilon^2), \end{aligned} \tag{A4}$$

which yields

$$d\Phi(u;v) = -\tfrac{1}{2}\mathcal{F}^{-1}[|k|\, \mathcal{F}[uv^* + vu^*]]. \tag{A5}$$

This completes the derivation of (A1).

[1] K. Dysthe, H. E. Krogstad, P. Müller, and P. Muller, Annu. Rev. Fluid Mech. **40**, 287 (2008).

[2] P. Muller, C. Garrett, and A. Osborne, Oceanography **18**, 66 (2005).

[3] U. Frisch, Ann. N.Y. Acad. Sci. **357**, 359 (1980).

[4] A. J. Majda and Y. Lee, Proc. Natl. Acad. Sci. USA **111**, 6548 (2014).

[5] W. Cousins and T. P. Sapsis, Phys. D (Amsterdam, Neth.) **280-281**, 48 (2014).

[6] W. Cai, S. Borlace, M. Lengaigne, P. Van Rensch, M. Collins, G. Vecchi, A. Timmermann, A. Santoso, M. J. McPhaden, L. Wu *et al.*, Nat. Climate Change **4**, 111 (2014).

[7] N. Chen, A. J. Majda, and D. Giannakis, Geophys. Res. Lett. **41**, 5612 (2014).

[8] F. Takens, Detecting strange attractors in turbulence, in *Dynamical Systems and Turbulence, Warwick 1980: Proceedings of a Symposium Held at the University of Warwick 1979/80* (Springer, Berlin, Heidelberg, 1981), pp. 366–381.

[9] T. Sauer, J. A. Yorke, and M. Casdagli, J. Stat. Phys. **65**, 579 (1991).

[10] T. Berry, D. Giannakis, and J. Harlim, Phys. Rev. E **91**, 032915 (2015).

[11] M. O. Williams, P. J. Schmid, and J. N. Kutz, Multiscale Model. Simul. **11**, 522 (2013).

[12] E. Chiavazzo, C. Gear, C. Dsilva, N. Rabin, and I. Kevrekidis, Processes **2**, 112 (2014).

[13] Z. Zhao and D. Giannakis (unpublished).

[14] S. Sargsyan, S. L. Brunton, and J. N. Kutz, Phys. Rev. E **92**, 033304 (2015).

[15] Z. Y. Wan and T. P. Sapsis, Phys. D (Amsterdam, Neth.) (2016).

[16] T. Berry and J. Harlim, Phys. D (Amsterdam, Neth.) **320**, 57 (2016).

[17] A. J. Majda and J. Harlim, *Filtering Complex Turbulent Systems* (Cambridge University Press, Cambridge, U.K., 2012).

[18] D. Giannakis and A. J. Majda, Proc. Natl. Acad. Sci. USA **109**, 2222 (2012).

[19] S. Bialonski, G. Ansmann, and H. Kantz, Phys. Rev. E **92**, 042910 (2015).

[20] N. Fenichel, J. Differ. Equations **31**, 53 (1979).

[21] J. Guckenheimer and P. Holmes, *Nonlinear Oscillations, Dynamical Systems, and Bifurcations of Vector Fields* (Springer Verlag, New York, 1983), Vol. 42.

[22] S. Wiggins, *Normally Hyperbolic Invariant Manifolds in Dynamical Systems*, Applied Mathematical Sciences Vol. 105 (Springer, New York, 1994).

[23] I. G. Kevrekidis, in *Supercomputer Research in Chemistry and Chemical Engineering*, ACS Symposium Series, Vol. 353, edited by K. F. Jensen and D. G. Truhlar (ACS Publications, Washington, DC, 1987), Chap. 16, pp. 284–294.

[24] I. G. Kevrekidis, B. Nicolaenko, and J. C. Scovel, SIAM J. Appl. Math. **50**, 760 (1990).

[25] M. Desroches, J. Guckenheimer, B. Krauskopf, C. Kuehn, H. M. Osinga, and M. Wechselberger, SIAM Rev. **54**, 211 (2012).

[26] A. Roberts, J. Guckenheimer, E. Widiasih, A. Timmermann, and C. K. R. T. Jones, J. Atmos. Sci. (2016), doi:10.1175/JAS-D-15-0191.1.

[27] G. Haller, Commun. Pure Appl. Math. **52**, 1 (1999).

[28] Z. Ren and S. B. Pope, Combust. Theory Modell. **10**, 361 (2006).

[29] H. Babaee and T. P. Sapsis, Proc. R. Soc. London, Ser. A **472**, 20150779 (2016).

[30] V. I. Arnold, *Ordinary Differential Equations* (Springer, Berlin, 1992) [translated by R. Cooke].

[31] J. M. Greene and J.-S. Kim, Phys. D (Amsterdam, Neth.) **24**, 213 (1987).

[32] L. Dieci and C. Elia, Math. Comput. Simul. **79**, 1235 (2008).

[33] G. Haller and T. Sapsis, SIAM J. Appl. Dyn. Syst. **9**, 611 (2010).

[34] U. Frisch, *Turbulence, The Legacy of A. N. Kolmogorov* (Cambridge University Press, Cambridge, U.K., 1996).

[35] M. Farazmand, J. Fluid Mech. **795**, 278 (2016).

[36] P. Constantin, C. Foias, and R. Temam, Phys. D (Amsterdam, Neth.) **30**, 284 (1988).

[37] P. K. Friz and J. C. Robinson, Phys. D (Amsterdam, Neth.) **148**, 201 (2001).

[38] N. K.-R. Kevlahan, J. Alam, and O. V. Vasilyev, J. Fluid Mech. **570**, 217 (2007).

[39] G. Berkooz, P. Holmes, and J. Lumley, Annu. Rev. Fluid Mech. **25**, 539 (1993).

[40] N. Platt, L. Sirovich, and N. Fitzmaurice, Phys. Fluids A **3**, 681 (1991).

[41] C. Marchioro, Commun. Math. Phys. **105**, 99 (1986).

[42] C. Foias, O. Manley, R. Rosa, and R. Temam, *Navier-Stokes Equations and Turbulence* (Cambridge University Press, Cambridge, U.K., 2001).

[43] G. J. Chandler and R. R. Kerswell, J. Fluid Mech. **722**, 554 (2013).

[44] R. Peyret, *Spectral Methods for Incompressible Viscous Flow*, Vol. 148 (Springer, Berlin, 2013).

[45] J. R. Dormand and P. J. Prince, J. Comp. App. Math. **6**, 19 (1980).

[46] A. Gelman, J. B. Carlin, H. S. Stern, D. B. Dunson, A. Vehtari, and D. B. Rubin, *Bayesian Data Analysis*, 3rd ed., Chapman & Hall/CRC Texts in Statistical Science (Taylor & Francis, Milton Park, U.K., 2013).

[47] P. J. Schmid, J. Fluid Mech. **656**, 5 (2010).

[48] P. J. Schmid, L. Li, M. Juniper, and O. Pust, Theor. Comput. Fluid Dyn. **25**, 249 (2011).

[49] P. J. Schmid, Exp. Fluids **50**, 1123 (2011).

[50] C. W. Rowley, I. Mezic, S. Bagheri, P. Schlatter, and D. S. Henningson, J. Fluid Mech. **641**, 115 (2009).

[51] K. K. Chen, J. H. Tu, and C. W. Rowley, J. Nonlinear Sci. **22**, 887 (2012).

[52] K. B. Dysthe, Proc. R. Soc. London, Ser. A **369**, 105 (1979).

[53] V. E. Zakharov, J. Appl. Mech. Tech. Phys. **9**, 190 (1968).

[54] T. B. Benjamin and J. E. Feir, J. Fluid Mech. **27**, 417 (1967).

[55] P. A. E. M. Janssen, J. Phys. Oceanogr. **33**, 863 (2003).

[56] M. A. Mohamad, W. Cousins, and T. P. Sapsis, J. Comp. Phys. **322**, 288 (2016).

[57] S. Cox and P. Matthews, J. Comput. Phys. **176**, 430 (2002).

[58] H. Berland, B. Skaflestad, and W. M. Wright, ACM Trans. Math, Software **33**, 4 (2007).

[59] H. Broer and F. Takens, *Dynamical Systems and Chaos* (Springer Science & Business Media, New York, 2010), Vol. 172.

[60] W. Cousins and T. P. Sapsis, Phys. Rev. E **91**, 063204 (2015).

[61] W. Cousins and T. P. Sapsis, J. Fluid Mech. **790**, 368 (2016).

[62] D. A. Egolf, I. V. Melnikov, W. Pesch, and R. E. Ecke, Nature (London) **404**, 733 (2000).

[63] M. Farazmand and G. Haller, Chaos **23**, 023101 (2013).

[64] V. I. Oseledec, Trans. Moscow Math. Soc. **19**, 197 (1968).

[65] F. Ginelli, P. Poggi, A. Turchi, H. Chaté, R. Livi, and A. Politi, Phys. Rev. Lett. **99**, 130601 (2007).